

MR Imaging of Renal Masses: Correlation with Findings at Surgery and Pathologic Analysis¹

TEACHING POINTS

See last page

Ivan Pedrosa, MD • Maryellen R. Sun, MD • Matthew Spencer, MD
Elizabeth M. Genega, MD • Aria F. Olumi, MD • William C. Dewolf, MD
Neil M. Rofsky, MD

Magnetic resonance (MR) imaging is useful in the characterization of renal masses. The MR imaging manifestations and pathologic diagnoses of 82 renal masses were reviewed and correlated. The MR imaging appearance of clear cell type renal cell carcinoma varies depending on the presence of cystic components, hemorrhage, and necrosis. Papillary renal cell carcinomas appear as well-encapsulated masses with homogeneous low signal intensity on T2-weighted images and homogeneous low-level enhancement after the intravenous administration of contrast material, or as cystic hemorrhagic masses with peripheral enhancing papillary projections. Transitional cell carcinoma may be seen as an irregular, enhancing filling defect in the pelvicaliceal system or ureter. Lymphomatous masses are usually hypointense relative to the renal cortex on T2-weighted images and enhance minimally on delayed gadolinium-enhanced images. Bulk fat is a distinguishing feature of angiomyolipoma. Oncocytoma has a variable and nonspecific appearance at MR imaging. MR imaging findings may allow the characterization of various renal masses and can provide valuable information for their clinical management.

©RSNA, 2008 • radiographics.rsna.org

Abbreviations: GRE = gradient-echo, H-E = hematoxylin-eosin, MIP = maximum-intensity-projection, RARE = rapid acquisition with relaxation enhancement, RCC = renal cell carcinoma, TCC = transitional cell carcinoma, 3D = three-dimensional

RadioGraphics 2008; 28:985–1003 • Published online 10.1148/rg.284065018 • Content Codes: **GU** **MR** **OI**

¹From the Departments of Radiology (I.P., M.R.S., M.S., N.M.R.), Pathology (E.M.G.), and Surgery (A.F.O., W.C.D.), Beth Israel Deaconess Medical Center, Harvard Medical School, 330 Brookline Ave, Boston, MA 02215. Recipient of an Excellence in Design award for an education exhibit at the 2003 RSNA Annual Meeting. Received February 14, 2006; revision requested March 24; final revision received August 20, 2007; accepted September 11. N.M.R. receives research support from GE Healthcare and Bayer (Berlex), is a consultant with EPIX Pharmaceuticals, and is on the advisory boards of Bayer (Berlex) and CAD Sciences; all remaining authors have no financial relationships to disclose. **Address correspondence to** I.P. (e-mail: ipedrosa@bidmc.harvard.edu).

©RSNA, 2008

Introduction

Magnetic resonance (MR) imaging is a useful tool for the characterization and presurgical staging of renal masses. Renal masses are being discovered with increasing frequency due to the large number of cross-sectional studies being performed in clinical practice. Accurate characterization of renal masses is essential to ensure appropriate case management and to assist in staging and prognosis.

Ultrasonography and computed tomography (CT) are commonly used for a variety of renal indications. MR imaging can be particularly helpful when renal lesions are detected but are not well characterized. A protocol for effective MR imaging of the kidney should maximize soft-tissue contrast, exploit the sensitivity of MR imaging to contrast material enhancement, and make full use of the multiplanar capability of this modality. The routine presurgical assessment of renal masses should include evaluation of the renal arterial supply and venous drainage. Correlating the anatomic findings and MR imaging signal intensity characteristics with the clinical features allows optimal diagnosis and staging.

We reviewed the MR imaging findings and pathologic diagnoses in 82 renal masses encountered over a 2-year period at our institution. Pathologic specimens were obtained at surgical biopsy ($n = 74$), core needle biopsy ($n = 7$), and urine cytologic examination ($n = 1$). The pathologic diagnoses included renal cell carcinoma (RCC) ($n = 68$ [clear cell, $n = 48$; papillary, $n = 15$; chromophobe, $n = 5$]), transitional cell carcinoma (TCC) ($n = 7$), lymphoma ($n = 2$), angiolipoma ($n = 1$), oncocytoma ($n = 1$), juxtaglomerular tumor ($n = 1$), solitary fibrous tumor ($n = 1$), and xanthogranulomatous pyelonephritis ($n = 1$). In this article, we discuss and illustrate the MR imaging appearances of these masses with emphasis on correlation with pathologic findings. In addition, we offer a comprehensive MR imaging protocol for the evaluation of renal masses and an MR urography protocol for the evaluation of suspected collecting system disease.

MR Imaging Protocol

MR imaging examinations are performed with a phased-array body coil with the patient supine. Each examination includes coronal half-

Fourier single-shot fast (or turbo) spin-echo images (SSFSE: GE Healthcare, Waukesha, Wis; HASTE: Siemens Medical Solutions, Malvern, Pa), axial dual-echo in-phase and opposed-phase gradient-echo (GRE) T1-weighted images, and coronal and sagittal three-dimensional (3D) fat-suppressed GRE T1-weighted images obtained prior to and following the intravenous administration of contrast material. Our standard imaging sequences and parameters, performed on 1.5-T systems, are listed in the Table and have been detailed previously (1). Each sequence is performed during a 20–24-second breath hold. Suspended respiration is most reproducible at end expiration, an essential consideration when subtraction postprocessing is performed, and is optimized with a brief coaching session prior to the examination. Oxygen administered via a nasal cannula greatly increases patients' breath-hold capability (2).

T2-weighted images are most helpful in distinguishing simple renal cysts from other lesions. A homogeneous hyperintense lesion with a thin wall on T2-weighted images can be accurately characterized as a simple cyst. Septa and solid nodules can be readily seen within cysts on T2-weighted images due to their relatively low signal intensity compared with the fluid contents within the cyst. Complicated renal cysts with hemorrhagic or proteinaceous contents may have heterogeneous or low signal intensity on T2-weighted images, whereas solid tumors have variable signal intensity.

The presence of enhancement within a renal lesion after the administration of gadolinium-based contrast material is the most reliable criterion for distinguishing solid masses from cysts at MR imaging (3). Comparison of pre- and postcontrast T1-weighted images is the key to the detection and characterization of renal lesions.

Precontrast T1-weighted images are also helpful in the characterization of certain aspects of cystic and solid lesions. Simple cysts are hypointense relative to the normal renal parenchyma on T1-weighted images due to their long relaxation time. Increased signal intensity within cysts may indicate the presence of hemorrhage or proteinaceous fluid (4). Similarly, hemorrhagic solid renal masses may display areas of increased signal intensity on T1-weighted images.

In-phase and opposed-phase GRE T1-weighted imaging is useful in the detection of

Teaching
Point

MR Imaging Protocol for Renal Masses

Sequence	Repetition Time (msec)	Echo Time (msec)	Flip Angle (°)	Section Thickness (mm)
Coronal SSFSE or HASTE	∞	62–64	130–155	5
Axial dual-echo in-phase/opposed-phase GRE T1-weighted*	170–180	2.2–2.8/4.4–5.3	80	6
Coronal and sagittal 3D fat-saturated GRE T1-weighted	4.0–5.0	1.3–2.0	12	3–4

*Single acquisition for in- and opposed-phase data sets.

intratumoral fat. It also provides valuable information for the diagnosis and characterization of incidental findings such as adrenal masses or hepatic steatosis.

Three-dimensional fat-saturated GRE T1-weighted sequences offer volumetric imaging with the ability to obtain meaningful multiplanar reformatted images (5). For the evaluation of renal masses, this sequence is performed in the coronal plane before and after the bolus administration of a single dose (0.1 mmol/kg) of extracellularly distributed gadolinium chelate contrast agent.

In our practice, gadopentetate dimeglumine (Magnevist; Berlex Laboratories, Wayne, NJ) is administered at a rate of 2 mL/sec and flushed with 20 mL of saline solution at the same rate. A timing examination is performed with a test bolus of 2 mL of gadopentetate dimeglumine followed by a 20-mL flush of saline solution. The procedure for timing the phases of acquisition has been previously described (6). Contrast material-enhanced images are obtained during the corticomedullary, nephrographic, and excretory phases following the initial contrast bolus. The corticomedullary phase is timed to the arterial peak and is also well suited to generate high-quality MR angiograms. A nephrographic phase acquisition is performed 40 seconds after the arterial peak. Finally, a sagittal 3D excretory phase fat-saturated GRE acquisition is performed through each kidney approximately 2 minutes after the administration of intravenous contrast material.

Each 3D data set acquired during the dynamic contrast-enhanced MR imaging examination can be used as a template from which the unenhanced data set is subtracted. Subtraction images can facilitate the detection of small enhancing

components within a cystic renal lesion, particularly when intralesional hemorrhagic or proteinaceous contents generate high signal intensity on unenhanced images, thereby rendering detection of enhancement within the lesion challenging. Similarly, subtraction images can help exclude the presence of enhancement in a hemorrhagic lesion. However, the value of subtraction images depends on proper coregistration of the post-contrast and unenhanced data sets, so that careful evaluation of the quality of the subtraction images is required at the time of interpretation. Ghosting artifact around the renal contour can be used as an index of the degree of misregistration. In our practice, end-expiratory breath-hold imaging is used, since it typically eliminates or minimizes discrepancies in respiration phase that can result in misregistration.

MR urograms are obtained in patients with suspected collecting system disease (eg, hematuria, suspicious urine cytologic findings). Our protocol includes a 3D fat-saturated GRE T1-weighted sequence with a high flip angle (40°–60°), with the latter providing saturation of the background signal. The resulting images are both viewed as source data and postprocessed as maximum-intensity-projection (MIP) images. This sequence is performed before and after the administration of gadolinium-based contrast material, during the excretory phase, following the three phases of the dynamic contrast-enhanced MR imaging examination. Concentrated gadolinium-based contrast material excreted in the urine at contrast-enhanced MR imaging is typically dark because the T2* effects outweigh the T1 relaxation effects. Immediately prior to the injection of gadolinium-based contrast material, 10 mg

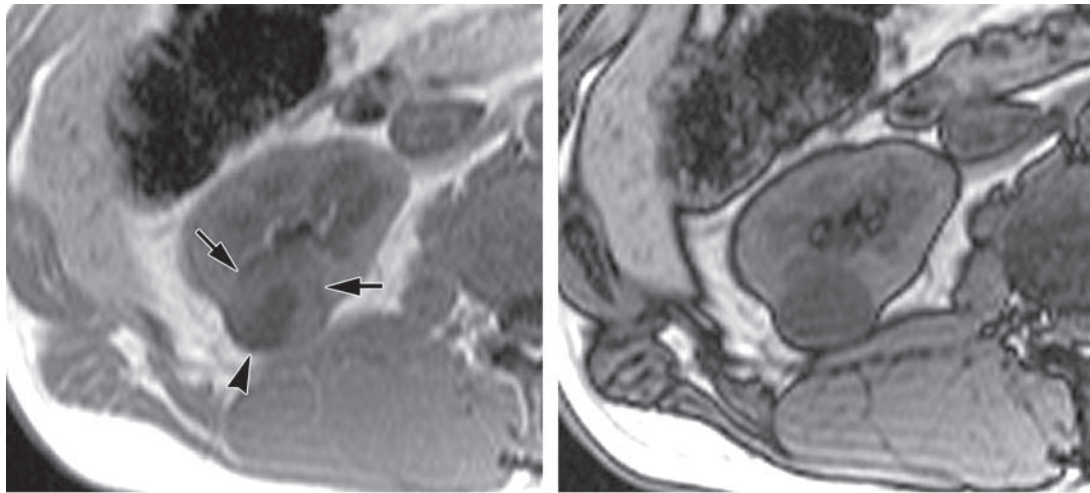
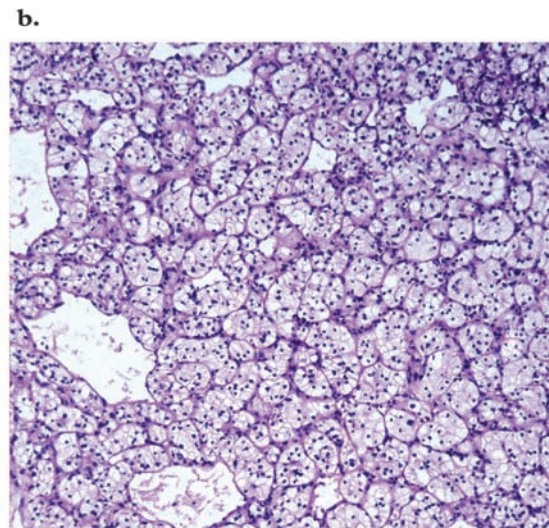


Figure 1. Clear cell RCC in a 52-year-old man. **(a)** Axial in-phase T1-weighted MR image shows a right renal mass with a thick rim of tumor (arrows). The signal intensity of the rim is similar to that of the renal cortex. A central low-signal-intensity area (arrowhead) is also present. **(b)** On an axial opposed-phase T1-weighted MR image, the mass appears homogeneous and is hypointense relative to the renal cortex. **(c)** Photomicrograph (original magnification, $\times 10$; hematoxylin-eosin [H-E] stain) helps confirm the presence of conventional (clear cell) RCC (Fuhrman grade 1–2). Clear cell cytoplasm may contain lipid that is responsible for the loss of signal intensity on opposed-phase MR images. Many tumor cells contain finely granular eosinophilic cytoplasm.



of furosemide is administered intravenously. The resulting diuresis permits distention of the collecting system and dilutes the excreted contrast material. The latter reduces the T2* effects of concentrated contrast material, resulting in increased signal intensity of the urine. **Coronal delayed 3D fat-saturated GRE T1-weighted images acquired after contrast material administration provide excellent MR urographic information for the assessment of urothelial disease.** A thick-slab single-shot fast spin-echo T2-weighted image (ie, SSFSE [GE Healthcare], HASTE [Siemens Medical Solutions], and rapid acquisition with relaxation enhancement [RARE] sequences) can be obtained and provides rapid assessment of the entire collecting system on a single image.

Renal Cell Carcinoma

Clear cell RCC is the most common type of RCC, accounting for approximately 65%–80% of

cases (7). At histologic analysis, clear cell RCC is composed of cells with optically clear cell cytoplasm due to accumulation of dissolved lipids and cholesterol. These tumors often contain cells with granular eosinophilic cytoplasm. Tumor cells are characteristically arranged in sheets, acini, or alveoli, and prominent thin-walled vasculature is characteristic (8). Hyalinization, fibrosis, and coagulative tumor necrosis are common (8). Cystic degeneration occurs in 4%–15% of RCCs (9,10).

Several grading systems based on tumor cell cytoplasmic or architectural features have been proposed (11). The Fuhrman grading system is the most widely accepted system and categorizes clear cell carcinoma into four groups: grade 1, tumor cells with small (approximately 10- μ m), round, uniform nuclei without nucleoli; grade 2, tumor cells with larger (approximately 15- μ m) nuclei with irregularities in outline and with nucleoli at high magnification ($\times 400$); grade 3, tumor cells with even larger (approximately 20- μ m) nuclei with an obviously irregular outline and

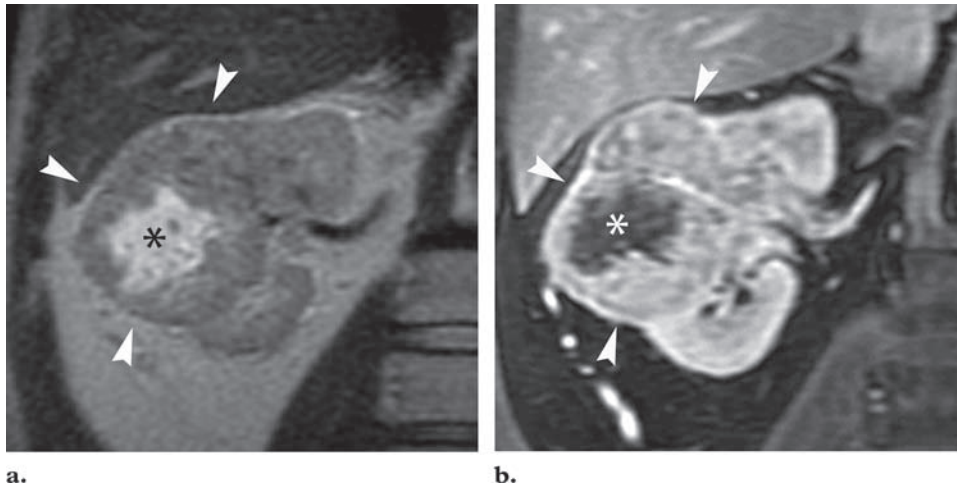


Figure 2. Clear cell RCC with central necrosis in a 58-year-old man. **(a)** Coronal single-shot fast spin-echo T2-weighted MR image shows a large mass in the midportion of the right kidney with an intermediate-signal-intensity rim (arrowheads) and a high-signal-intensity central area (*). **(b)** Coronal gadolinium-enhanced 3D nephrographic phase fat-saturated GRE T1-weighted MR image helps confirm the presence of a solid rim of enhancing tumor (arrowheads) at the periphery of the mass and a central area of necrosis (*) that does not enhance. Histopathologic analysis performed after nephrectomy revealed high-grade clear cell carcinoma with central necrosis.

with prominent larger nucleoli even at low magnification ($\times 100$); and grade 4, tumor cells with bizarre, multilobed nuclei with heavy clumps of chromatin (11). A correlation between Fuhrman grade and prognosis has been reported, with a poorer prognosis for patients with high-grade carcinoma (11). Although this grading system was developed to characterize clear cell RCC, its use has been expanded to include other subtypes (eg, papillary RCC).

Clear cell RCC is associated with a poorer prognosis than either papillary or chromophobe RCC (8,12). Sarcomatoid and rhabdoid differentiations of clear cell RCC are also associated with a poorer prognosis (8).

The MR imaging appearance of clear cell RCC varies depending on the presence of hemorrhage and necrosis. Clear cell RCC most frequently demonstrates a signal intensity similar to that of the renal parenchyma on T1-weighted images and increased signal intensity on T2-weighted images. **Loss of signal intensity within the solid portions of clear cell RCCs on opposed-phase images compared with in-phase images (Fig 1) is due to cytoplasmic fat and has been observed in up to 60% of these tumors (13).** Central necrosis is common and is typically seen as a homogeneous hypointense area in the center of the mass on T1-weighted images. On T2-weighted images, necrosis tends to have moderate to high signal intensity (Fig 2), although

occasionally it may appear hypointense (14). In the presence of central necrosis, a solid rim of tumor is frequently seen at the periphery of the mass. Postcontrast images demonstrate lack of enhancement in areas of necrosis and marked enhancement in the viable components of the tumor.

Intratumoral hemorrhage may occur and has a variable appearance depending on the stage of degradation of the component blood products. Subacute to chronic hemorrhage generally demonstrates high signal intensity on both T1- and T2-weighted images. Long-standing hemorrhage, which predominantly contains hemosiderin, is typically hypointense on both T1- and T2-weighted images (15).

A hypointense rim or pseudocapsule may be seen on both T1- and T2-weighted images and is thought to be related to compression of the adjacent renal parenchyma by the expanding tumor, although occasionally a fibrous capsule can be seen at pathologic analysis. Interruption of this pseudocapsule correlates with advanced stage (invasion of perirenal fat) and higher nuclear grade (16).

Clear cell RCC tends to be hypervascular, with heterogeneous enhancement during the arterial phase. Renal vein tumor thrombus can be seen with aggressive higher-stage tumors.

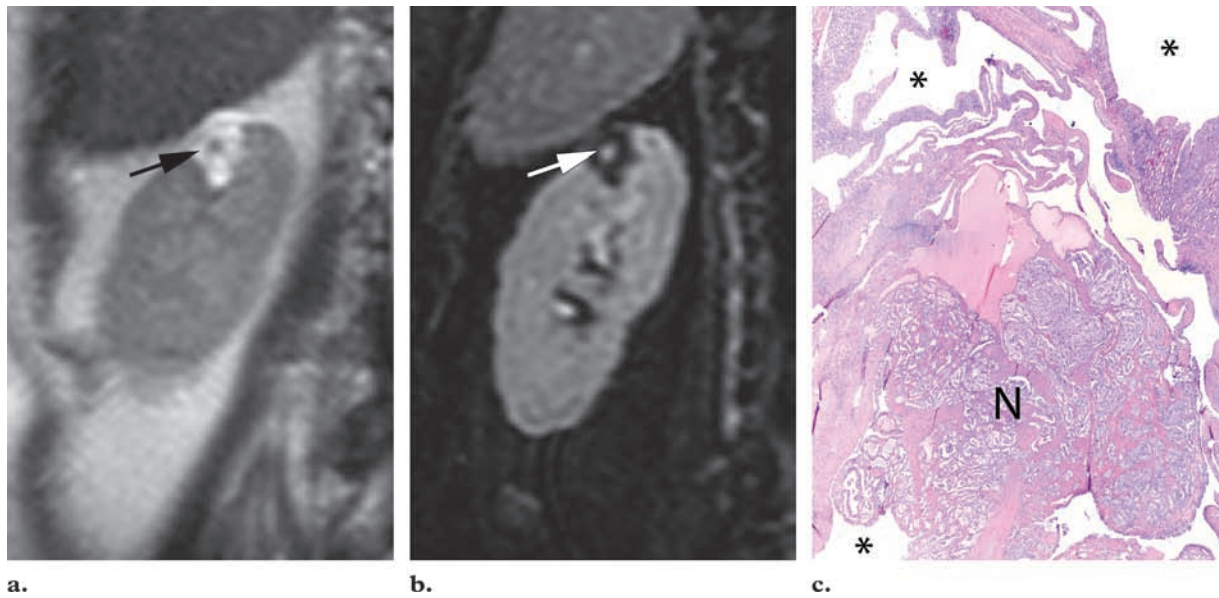


Figure 3. Predominantly cystic RCC. (a) Coronal single-shot fast spin-echo T2-weighted MR image shows a mass in the upper pole of the right kidney, with predominantly high signal intensity that is suggestive of fluid contents. A small nodule with intermediate signal intensity (arrow) is noted centrally at the confluence of thin septa. (b) Coronal subtraction image (postcontrast nephrographic phase data – precontrast data) shows enhancement of the small central nodule (arrow) within the mass. (c) Photomicrograph (original magnification, $\times 2$; H-E stain) helps confirm the presence of a small solid nodule (*N*) within a largely cystic (*) clear cell RCC.

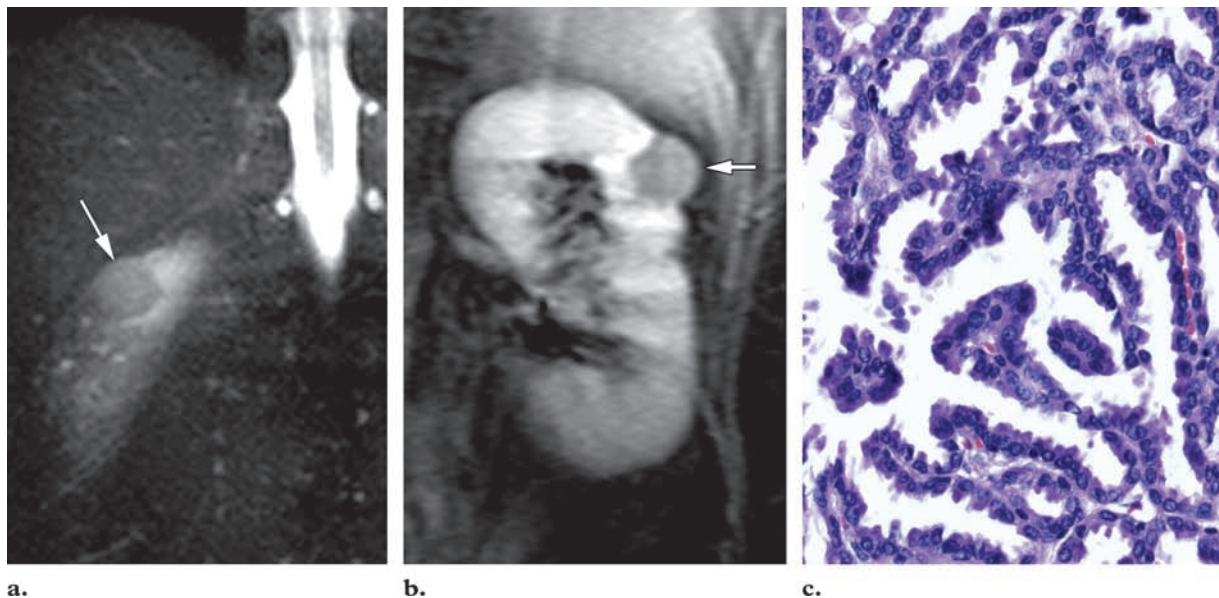
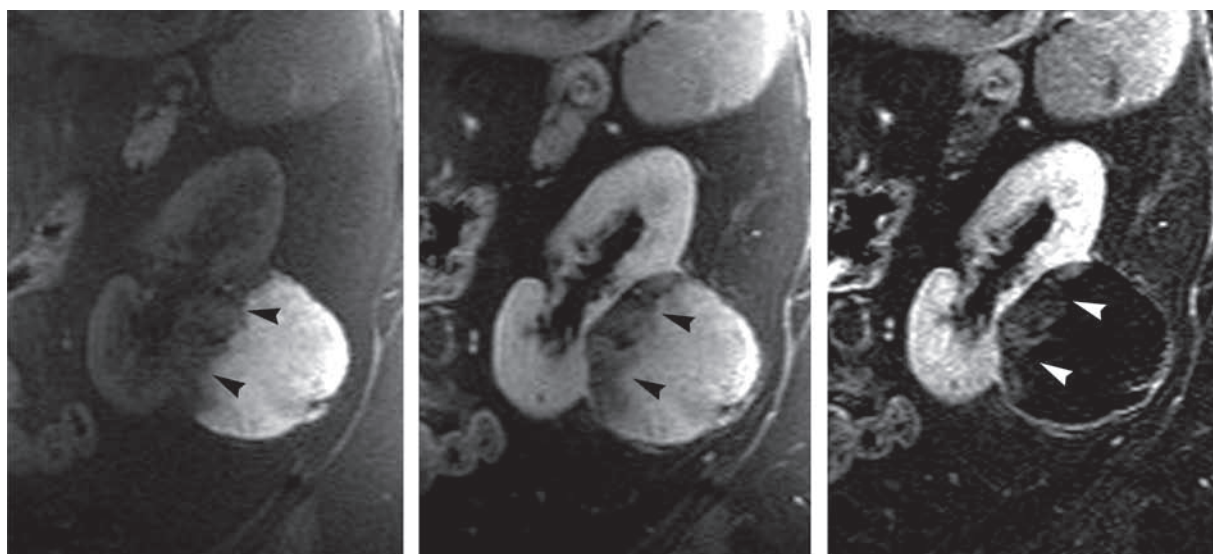


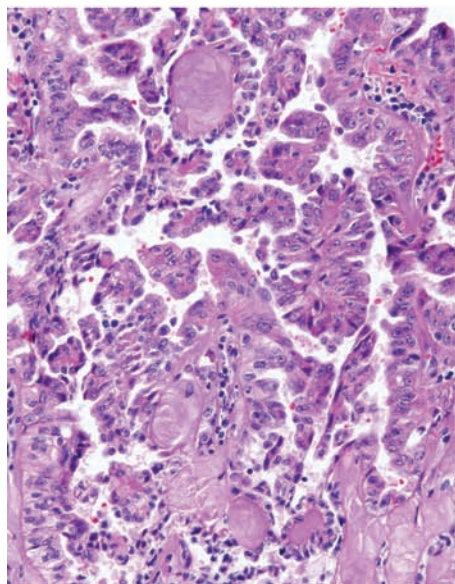
Figure 4. Low-grade papillary RCC in a 70-year-old woman. (a) Coronal fat-saturated steady-state fast spin-echo T2-weighted MR image shows a small mass (arrow) in the upper pole of the right kidney. The mass is homogeneously hypointense relative to the adjacent renal parenchyma. (b) On a sagittal oblique subtraction image, the mass (arrow) enhances homogeneously and less than the normal right kidney. (c) Photomicrograph (original magnification, $\times 40$; H-E stain) shows papillae lined by cytologically low-grade cells with a small amount of cytoplasm and relatively uniform nuclei, findings that are consistent with a type I papillary RCC (Fuhrman grade 2).



a.

b.

c.



d.

Figure 5. High-grade papillary RCC in a 70-year-old man. **(a)** Sagittal unenhanced 3D fat-saturated GRE T1-weighted MR image shows a large, heterogeneous mass. The hyperintense component is consistent with blood products. The peripheral anterior area of the mass (arrowheads) is clearly hypointense relative to the hemorrhagic component. **(b)** On a sagittal delayed venous phase image obtained after the administration of gadolinium-based contrast material, the peripheral area (arrowheads) is slightly less hypointense relative to the larger central portion, a finding that suggests the presence of an enhancing solid component. Determination of tumor enhancement is challenging on the basis of these findings alone. **(c)** On a post-contrast subtraction image (data in **b** – data in **a**), the enhancement of the peripheral component of the mass (arrowheads) is readily visible. **(d)** Photomicrograph (original magnification, $\times 20$; H-E stain) shows papillae lined by cells with abundant eosinophilic cytoplasm and pleomorphic nuclei with prominent nucleoli. Necrosis was present elsewhere. These findings are consistent with a type II papillary RCC (Fuhrman grade 3).

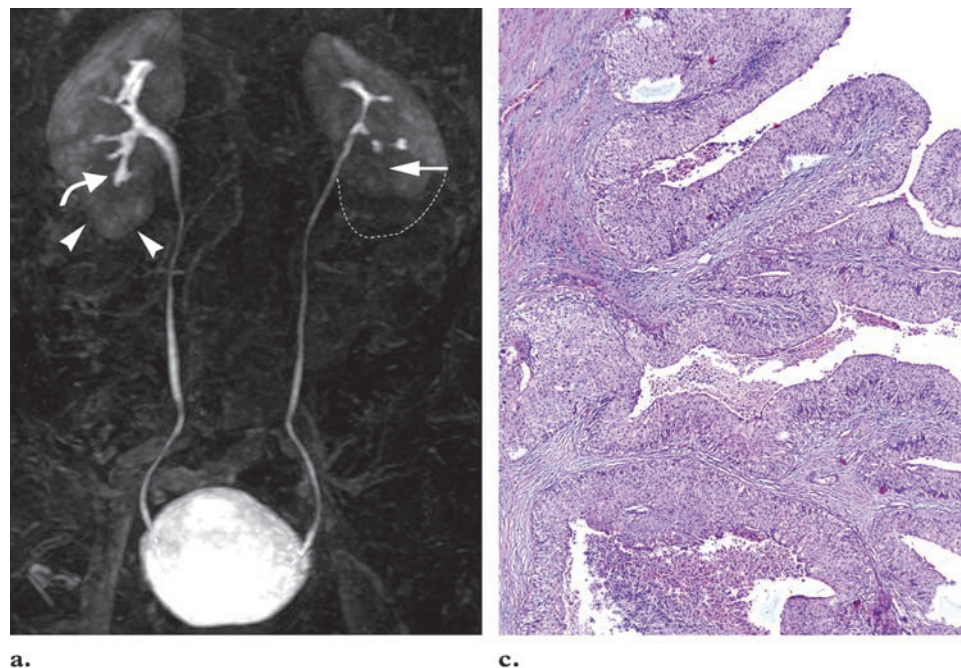
Clear cell carcinomas can also be predominantly cystic with only scant areas of solid enhancing component (Fig 3).

Papillary RCC accounts for approximately 10%–15% of all RCCs and may be multifocal (17). Papillary RCC is divided into two histologic types: basophilic and eosinophilic. Type I (basophilic) papillary tumors are composed of small cuboidal cells with uniform nuclei covering thin papillae (18). At MR imaging, they demonstrate homogeneous low signal intensity on T2-weighted images, with homogeneous low-level enhancement after intravenous contrast material administration (Fig 4) (19,20). Necrosis and hemorrhage may be present in low-grade type I tumors and, when present, result in a more het-

erogeneous appearance. Type II (eosinophilic) papillary RCCs consist of large eosinophilic cells with pleomorphic nuclei. At MR imaging, they usually have a more complex appearance than do low-grade papillary tumors, with hemorrhage and necrosis. Enhancing papillary projections at the periphery of a cystic hemorrhagic mass are common and can be better depicted on subtraction images (Fig 5). A fibrous capsule is typically present in papillary RCCs. Type I tumors tend to be of lower nuclear grade than type II tumors. However, the histologic subtype is an independent predictor of prognosis regardless of the nuclear grade (17).

Chromophobe renal tumors account for approximately 4%–11% of RCCs (21,22) and are postulated to arise from the intercalated cells of

Figure 6. Infiltrative papillary TCC. **(a)** Coronal contrast-enhanced MIP image obtained after the administration of 10 mg of furosemide clearly depicts the lower calices (straight arrow) and the lower pole (dotted line) of the left kidney. Note the normal enhancement of the lower pole of the right kidney (arrowheads) and the excreted contrast material in the lower pole calix (curved arrow). **(b)** Coronal contrast-enhanced 3D arterial phase image shows an infiltrating mass that involves the renal sinus (arrow) and the lower pole (arrowheads) of the left kidney. **(c)** Photomicrograph (original magnification, $\times 4$; H-E stain) shows the tumor composed of fibrovascular cores lined by low-grade cytologically malignant cells, findings that are consistent with a low-grade papillary urothelial carcinoma. A focus of invasive carcinoma in the renal sinus was also present.



the renal cortex. Tumor cells are round to polygonal and have well-defined cytoplasm borders, pale eosinophilic cytoplasm with a fine reticular pattern, and perinuclear haloes (8). At microscopic analysis, tumor cells usually demonstrate a pattern of solid growth. MR imaging may show cystic changes within a solid tumor. Central necrosis may be absent even in very large chromophobe carcinomas. Although the imaging features of chromophobe RCC can be identical to those of clear cell RCC, the chromophobe subtype tends to have a better prognosis (8).

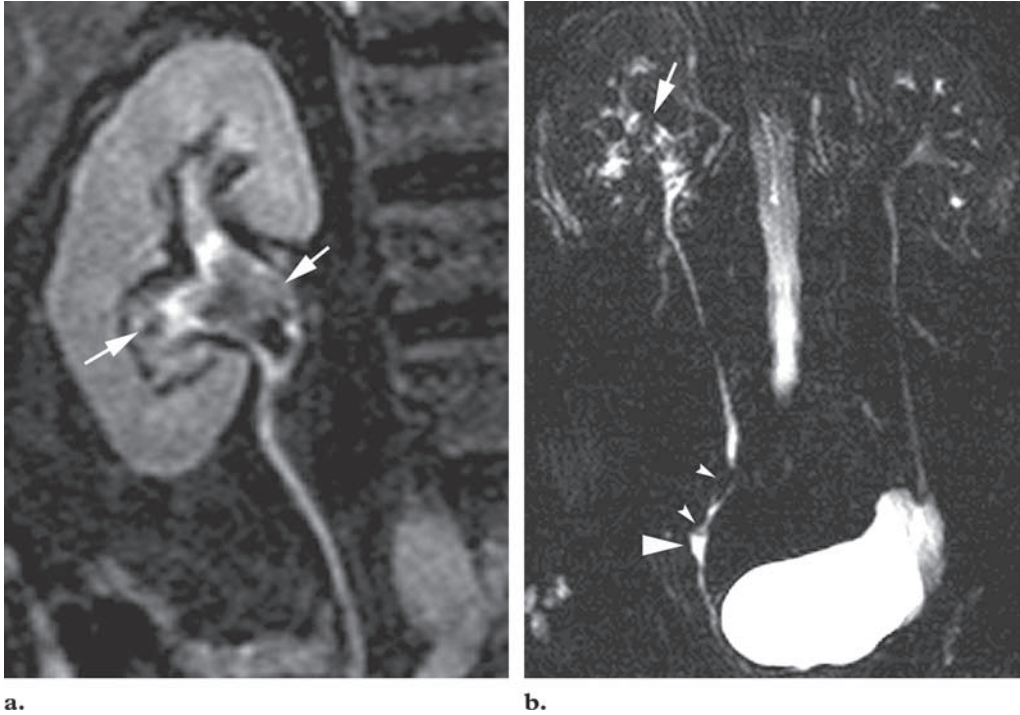
Transitional Cell Carcinoma

TCC is much less common in the upper tract than in the bladder. However, it accounts for 90% of all tumors that arise from the renal pelvic urothelium (23). TCC is divided into two histologic subtypes: papillary and nonpapillary. Both subtypes consist of transitional epithelium with varying degrees of cellular and architectural



atypia, arranged on thin connective tissue cores in the papillary subtype and forming thickened urothelium in the nonpapillary subtype. Papillary TCC is the more common subtype. TCC is frequently multifocal and may involve any part of the collecting system. Hematogenous spread is less common than with RCC, but lymphatic metastases occur early. Although high-grade tumors are more common in the upper tract than in the bladder, it has been suggested that stage,

Figure 7. TCC in a 74-year-old man. **(a)** Magnified thin-section 3D T1-weighted view of the right kidney on a coronal subtraction image shows enhanced filling defects within the renal pelvis (arrows), findings that are consistent with TCC. **(b)** T2-weighted MR urogram (thick-slab RARE sequence, repetition time msec/echo time msec = 2800/1100, flip angle = 160°, section thickness = 40 mm) shows filling defects in the renal pelvis (arrow) and lower ureter (small arrowheads). Note the dilatation of the ureter (large arrowhead) distal to the filling defects (“goblet sign”). Multifocal tumor in the renal pelvis and distal ureter was confirmed at surgery and pathologic analysis.



rather than tumor grade, is the main predictor of prognosis for urothelial tumors of the upper tract (24–26).

TCCs are typically isointense relative to the renal medulla on T1-weighted images, making the detection of small tumors in the collecting system virtually impossible. Larger infiltrative tumors may obliterate the fat in the renal sinus, which may be appreciated on T1-weighted images without the use of fat-saturation techniques. This appearance may mimic the so-called faceless kidney, described in the presence of a duplicated collecting system (27). Coronal contrast-enhanced T1-weighted images are helpful in distinguishing between these two conditions. Bright signal intensity due to urine in the collecting system on T2-weighted images provides excellent soft-tissue contrast for the detection of these tumors, which are characteristically seen as hypointense filling defects. Infiltrative TCC can be seen on single-shot T2-weighted images as a hypointense soft-tissue mass infiltrating the renal parenchyma, which has intermediate signal intensity. On postcontrast images, infiltrative TCC

may be recognized as a hypoenhancing mass, although avid enhancement may occur. MIP images generated from the postcontrast acquisition provide a display format that resembles intravenous pyelograms and may render these findings more conspicuous through comparison with the contralateral kidney (Fig 6).

Enhancement of a focal filling defect in the collecting system is strongly suggestive of a TCC. Differentiation between blood clots and enhancing filling defects is best accomplished by reviewing subtracted data sets (Fig 7).

Tumor may extend into the renal parenchyma and appear as an infiltrating mass, although the reniform shape of the kidney is usually preserved even in the presence of large tumors. Findings may be subtle, with only pelvic or ureteral wall thickening. Hydronephrosis proximal to the lesion is usually present unless the collecting system is completely filled by tumor. Occasionally, TCC may extend inferiorly within the periureteral

Teaching Point

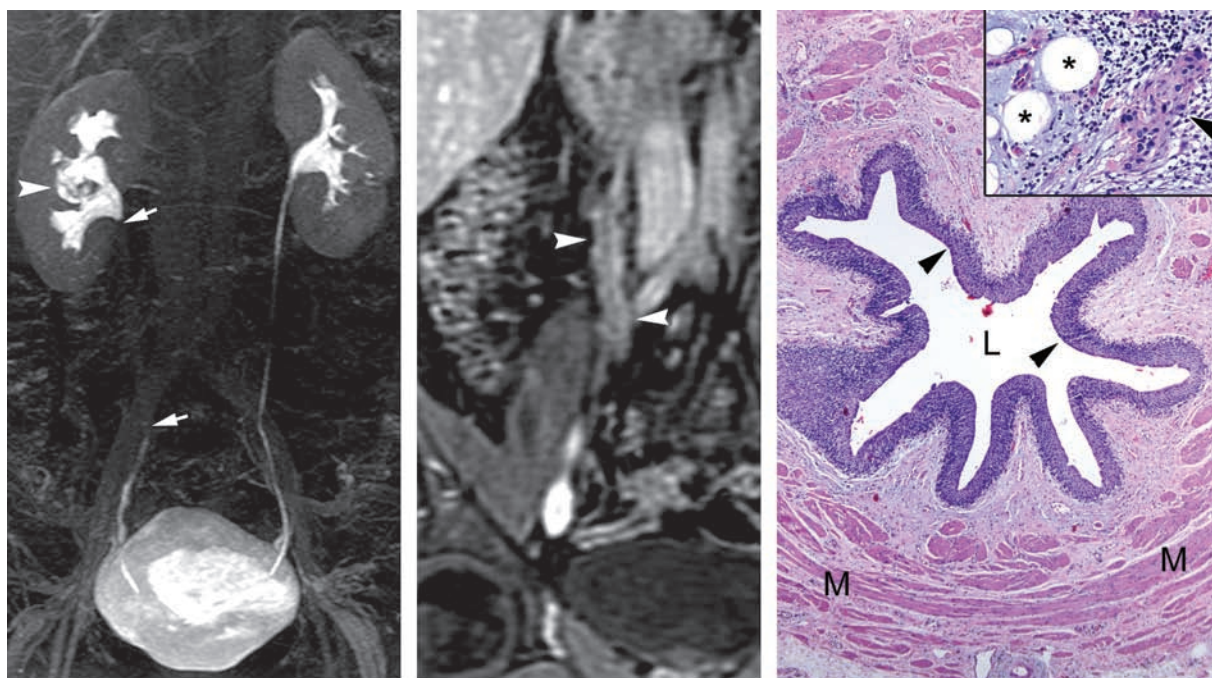


Figure 8. TCC with periureteral involvement in a 54-year-old woman with right flank pain. Retrograde ureteroscopy showed an “apple core” lesion in the upper collecting system but no abnormalities in the midureter. **(a)** Coronal MIP image from contrast-enhanced MR urographic data shows mild right hydronephrosis with blunting of the calices in the middle of the right kidney and an irregular mass (arrowhead) in the central portion of the kidney. The proximal and middle portions of the ureter are not visualized (arrows). **(b)** Coronal contrast-enhanced 3D nephrographic phase fat-saturated GRE T1-weighted MR image shows thickening and irregularity of the proximal ureter (arrowheads). **(c)** Photomicrograph (original magnification, $\times 4$; H-E stain) shows tumor cells that extend inferiorly from the TCC in the renal pelvis (not shown), outside the ureteral lumen (*L*), and along the periureteral fat. The midureter is lined by normal urothelium (arrowheads) and the tunica muscularis (*M*). The photomicrograph in the inset (original magnification, $\times 20$; H-E stain) shows invasive urothelial carcinoma (arrowhead) adjacent to adipocytes (*) within the periureteral fat. Periureteral involvement from a primary pelvic TCC is uncommon but represents a potential cause of false-negative results at retrograde ureteroscopy.

fat, encasing the ureter without tumor involvement of the ureteral mucosa (Fig 8).

The entire collecting system must be evaluated in patients with upper tract TCC because of the high prevalence of secondary foci of tumor. A cup-shaped dilatation of the ureter just distal to a focus of TCC of the ureter—also referred to as the goblet sign, chalice sign, or Bergman sign—may be seen (Fig 7). This finding is secondary to distal propulsion of a slow-growing intraluminal polypoid mass during ureteral peristalsis (28).

Lymphoma

Renal involvement by lymphoma may be due to hematogenous dissemination or contiguous extension of retroperitoneal disease; primary renal lymphoma is rare. Non-Hodgkin lymphoma is much more common in the kidney than is Hodgkin disease. At pathologic analysis, an initial growth of lymphomatous cells occurs in the

interstitium, with the nephrons, collecting ducts, and blood vessels serving as a framework for tumor expansion (29,30). With continued growth, there is parenchymal compression and destruction, with masslike proliferation (29). A number of appearances may be seen at imaging.

The most common pattern of lymphomatous involvement of the kidney (60% of cases) consists of one or more homogeneous masses with low-level enhancement (Fig 9) (23,30–32). A bulky retroperitoneal mass, which may extend directly to and encase one or both kidneys, is the second most common pattern (25%–30% of cases) (30,31,33). Less commonly seen is an infiltrative pattern, characterized by nephromegaly without disruption of the renal contour. Involvement of the perinephric space by lymphoma is uncommon but strongly suggests the diagnosis (Fig 10). There may be peripelvic and periureteral disease that manifests as wall thickening and enhancement (Fig 11). Following treatment, imaging findings may resolve with minimal residual scarring.

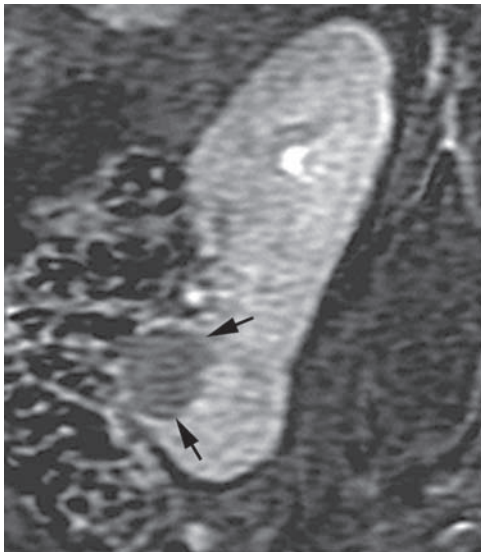


Figure 9. Renal lymphoma in a 31-year-old man with recurrent mediastinal lymphoma and an enlarging renal mass. Sagittal contrast-enhanced fat-saturated subtraction (excretory phase data – precontrast data) T1-weighted MR image reveals a well-defined, homogeneous, hypoenhancing mass (arrows). Lymphoma was confirmed with percutaneous biopsy.

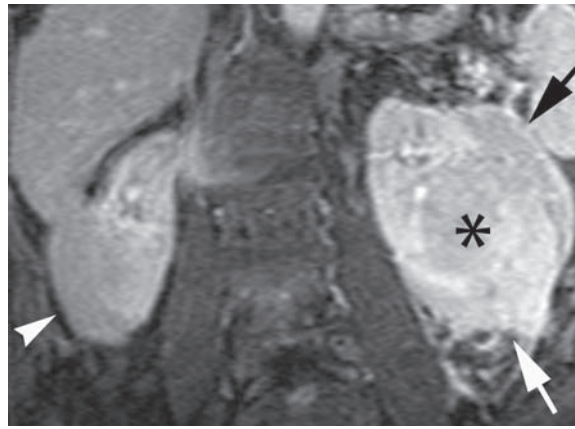
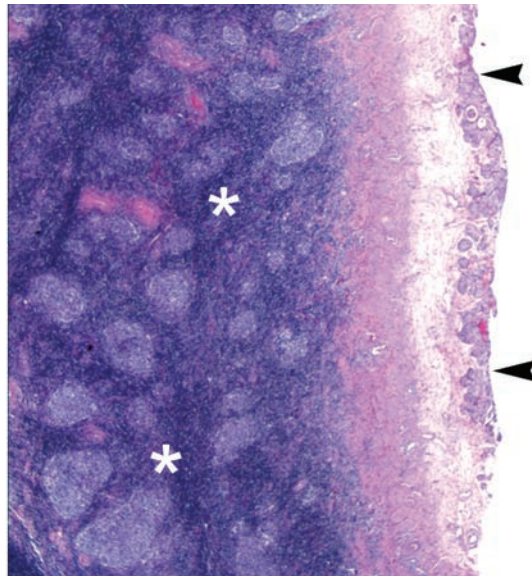


Figure 10. Retroperitoneal B-cell lymphoma in an 88-year-old man. Coronal contrast-enhanced 3D excretory phase fat-saturated GRE T1-weighted MR image shows a large mass in the left kidney (*) extending into the perinephric fat (arrows). In addition, a soft-tissue mass (arrowhead) is seen arising from the lower pole of the right kidney and extending into the perinephric fat. These findings are virtually diagnostic for lymphoma. Results of percutaneous biopsy confirmed low-grade B-cell lymphoma.



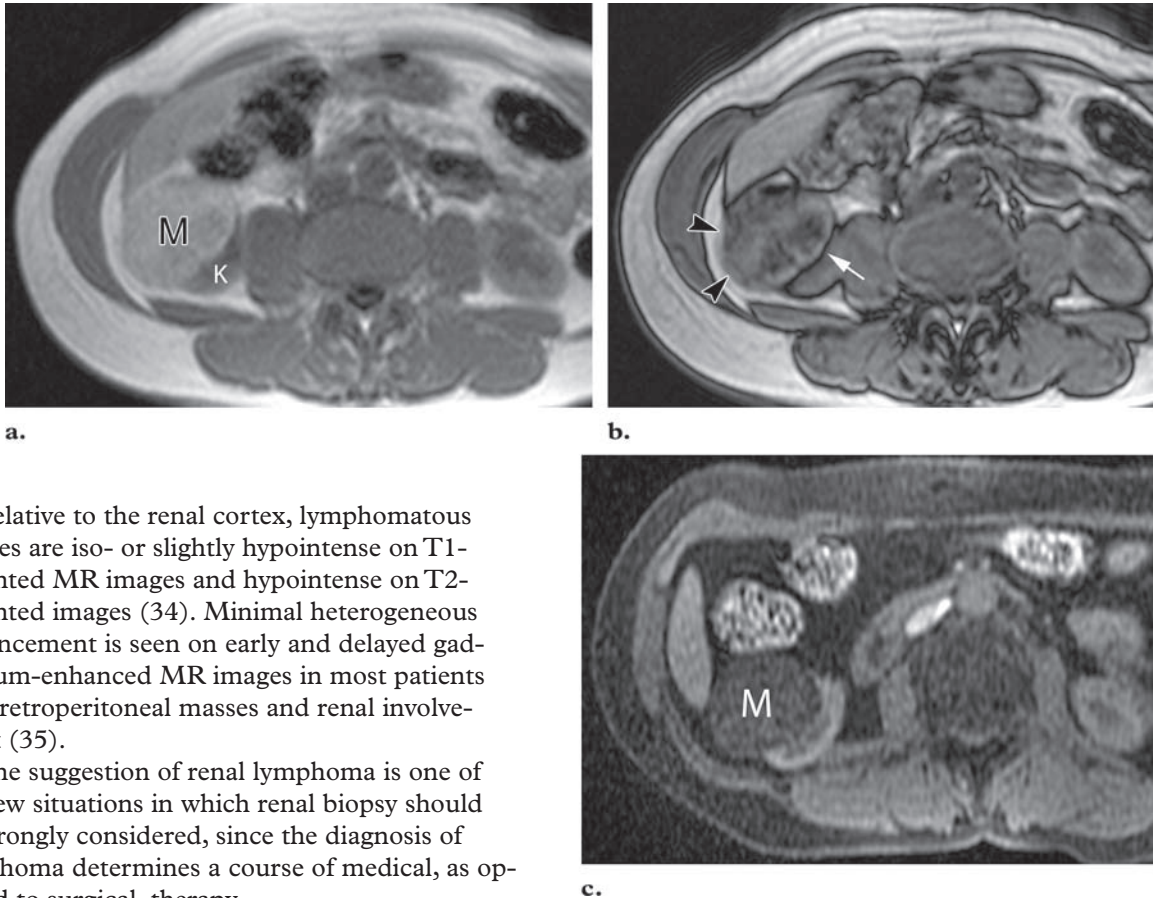
a.



b.

Figure 11. Non-Hodgkin follicular B-cell lymphoma involving the renal pelvic wall and renal sinus in a 58-year-old woman. (a) Sagittal contrast-enhanced thin-section subtraction (excretory phase data – precontrast data) T1-weighted MR image shows soft-tissue thickening and enhancement of the wall of the renal pelvis (arrowheads). Percutaneous biopsy of the renal pelvic wall was nondiagnostic, and the patient underwent a right nephrectomy. (b) Photomicrograph (original magnification, $\times 2$; H-E stain) shows the renal pelvis lined by normal urothelium (arrowheads), with non-Hodgkin follicular B-cell lymphoma (*) involving the renal pelvic wall.

Figure 12. Angiomyolipoma in a 54-year-old woman. **(a)** Axial in-phase GRE T1-weighted MR image shows a large mass (*M*) arising from the lower pole of the right kidney (*K*). The mass has higher signal intensity than the renal parenchyma. **(b)** Axial opposed-phase GRE T1-weighted MR image shows a mild decrease in signal intensity in some areas of the mass due to the intravoxel coexistence of fat and water protons. However, there is persistent high signal intensity in other areas of the mass, a finding that suggests the presence of bulk fat. A characteristic “India ink” artifact is seen at the fat-water interface between the mass and the kidney (arrow). Note that this artifact is not present in the exophytic portion of the mass (arrowheads), which represents a fat-fat interface between retroperitoneal fat and fat in the mass itself. **(c)** Axial 3D GRE T1-weighted MR image obtained with frequency-selective fat saturation shows diffuse suppression of signal intensity within the mass (*M*), thereby helping confirm the presence of bulk fat. Demonstration of bulk fat in a renal mass is virtually diagnostic for angiomyolipoma.



Relative to the renal cortex, lymphomatous masses are iso- or slightly hypointense on T1-weighted MR images and hypointense on T2-weighted images (34). Minimal heterogeneous enhancement is seen on early and delayed gadolinium-enhanced MR images in most patients with retroperitoneal masses and renal involvement (35).

The suggestion of renal lymphoma is one of the few situations in which renal biopsy should be strongly considered, since the diagnosis of lymphoma determines a course of medical, as opposed to surgical, therapy.

Benign and Uncommon Masses

Angiomyolipoma

Angiomyolipomas are hamartomas containing varying proportions of fat, smooth muscle, and thick-walled blood vessels (36).

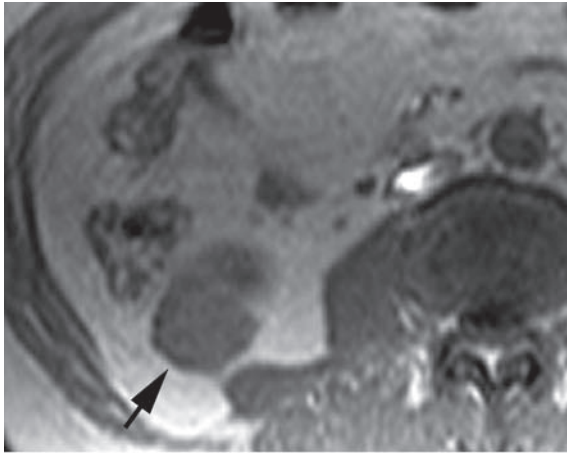
Angiomyolipoma can cause significant signs and symptoms, including pain, gross hematuria, anemia, and hypertension (37,38). Tumors greater than 4 cm carry an increased risk for potentially life-threatening hemorrhage (Wunderlich syndrome), which has been reported in up to 10% of these patients (38,39).

A reliable diagnosis of angiomyolipoma can be made when fat is unequivocally demonstrated in a renal mass (40). Angiomyolipomas with a predominant fatty component are isointense relative to fat with all MR imaging sequences (3), and their signal intensity is typically higher than that of the renal parenchyma on T1-weighted images (41). However, **the most reliable demonstration of bulk fat within an angiomyolipoma can be achieved by comparing images obtained with the same imaging parameters before and after applying a selective fat-suppression pulse (Fig 12) (3).**

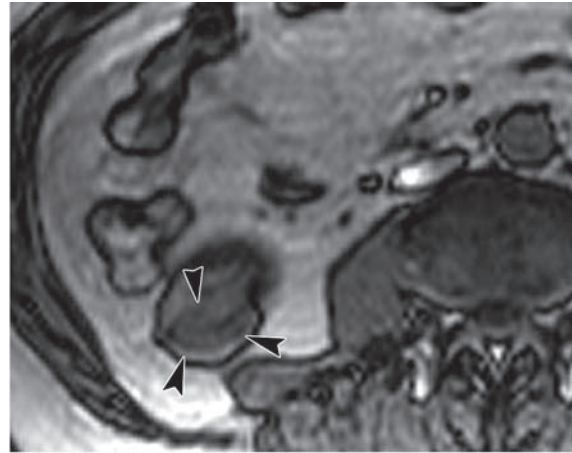
The use of in-phase and opposed-phase imaging is also helpful in the diagnosis of angiomyolipoma (1,42,43). In predominantly fatty angio-

**Teaching
Point**

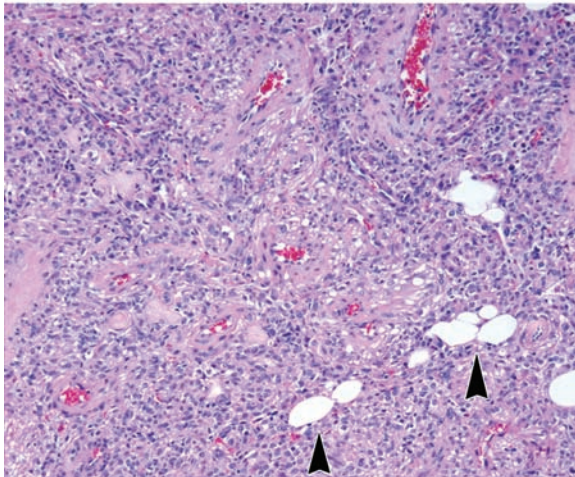
Figure 13. Lipid-poor angiomyolipoma in a 54-year-old woman. **(a)** Axial in-phase T1-weighted MR image shows a mass (arrow) arising from the lower pole of the right kidney. The mass has homogeneous signal intensity similar to that of the psoas muscle. **(b)** Corresponding opposed-phase image demonstrates only minimal loss of signal intensity in the posterior aspect of the lesion (arrowheads). No gross fat was detected in the lesion on frequency-selective fat-saturated T1-weighted images. **(c)** Photomicrograph (original magnification, $\times 10$; H-E stain) shows the mass composed of smooth muscle surrounding thick-walled vessels, along with rare, scattered mature adipocytes (arrowheads), findings that are consistent with an angiomyolipoma. Making the diagnosis of angiomyolipoma at MR imaging is virtually impossible in the absence of detectable macroscopic fat. Clear cell RCC should be included in the differential diagnosis when only intracellular fat is visualized.



a.



b.



c.

myolipoma, a characteristic India ink artifact is seen at the interface between the mass and the normal renal parenchyma on opposed-phase T1-weighted images, whereas the central portions of the lesion do not demonstrate changes in signal intensity compared with the in-phase images. This finding is particularly helpful in facilitating the diagnosis of angiomyolipoma in very small lesions, in which the direct comparison of T1-weighted images obtained without and with selective fat suppression may be more challenging (1,43).

The appearance of angiomyolipoma on T2-weighted images is variable and depends on the

amount of bulk fat present in the lesion. Angiomyolipoma composed predominantly of fat would demonstrate homogeneous high signal intensity at single-shot T2-weighted imaging. The signal intensity of these masses can be saturated with the use of frequency-selective fat-saturation techniques. Lipid-poor angiomyolipomas frequently demonstrate homogeneous low signal intensity relative to the renal parenchyma on T2-weighted images.

In angiomyolipoma with scant amounts of fat, the intravoxel coexistence of fat and water can be seen as a loss of signal intensity throughout the entire mass on opposed-phase images compared with in-phase images. This finding may be the only clue to the diagnosis of lipid-poor angiomyolipoma, in which bulk fat cannot be appreciated (Fig 13). It has been suggested that distinction between lipid-poor angiomyolipoma and other renal neoplasms can be made based on decreased signal intensity of the mass at opposed-phase imaging compared with in-phase imaging (44). However, caution must be exercised when the diagnosis of angiomyolipoma is made based on this phenomenon alone, since a loss of signal intensity on opposed-phase images can also be seen in clear cell RCC with small amounts of

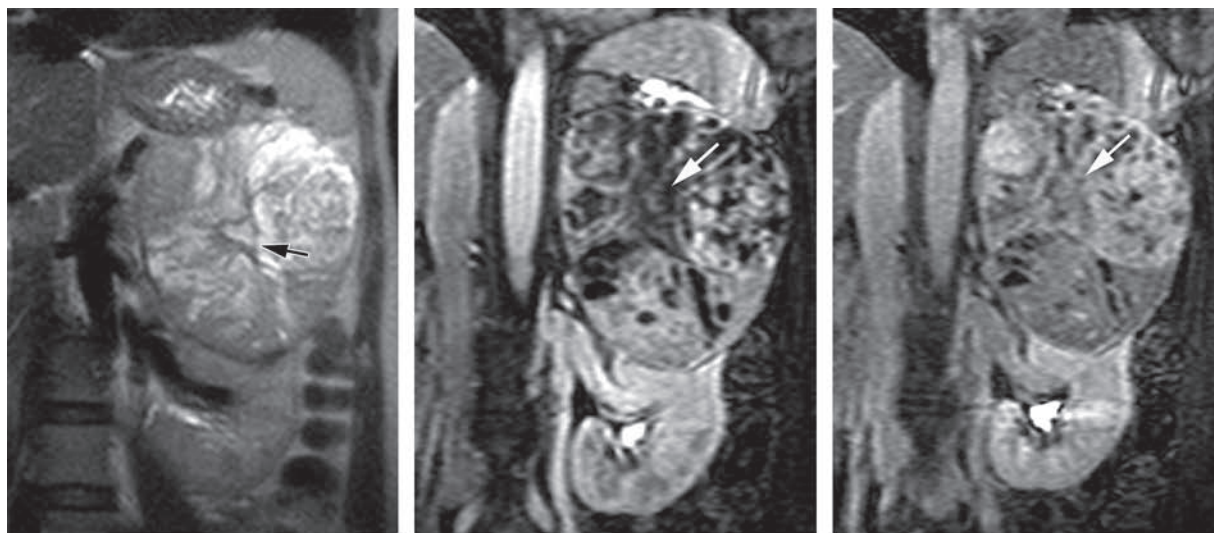


Figure 14. Oncocytoma in a 42-year-old woman. **(a)** Coronal single-shot fast spin-echo MR image shows a large, well-defined mass with heterogeneous signal intensity and a central cleft (arrow). **(b, c)** Coronal contrast-enhanced nephrographic phase **(b)** and delayed excretory phase **(c)** MR images show the mass with heterogeneous enhancement. The central cleft (arrow) is enhanced on the delayed image, thereby excluding necrosis. There are no features to reliably help distinguish oncocytoma from RCC. Oncocytoma was confirmed at histopathologic analysis performed after left nephrectomy.

intracellular fat (13). Furthermore, detection of fat with current MR imaging techniques may be virtually impossible in some lipid-poor angiomyolipomas.

In our experience, the presence of central necrosis may be helpful in suggesting the diagnosis of RCC, since medium to large clear cell RCCs frequently demonstrate central necrosis, a finding that is very rare in angiomyolipoma. The presence of scant amounts of intratumoral fat at opposed-phase and in-phase imaging with homogeneous hypointensity on T2-weighted images is suggestive of lipid-poor angiomyolipoma. However, pre-surgical differentiation of lipid-poor angiomyolipoma from clear cell RCC with MR imaging or other imaging techniques presents a diagnostic challenge that remains unresolved. Percutaneous biopsy could be contemplated prior to surgical excision in these circumstances, although surgical excision and histopathologic evaluation may occasionally be required to establish the correct diagnosis.

Contrast-enhanced MR imaging does not help differentiate angiomyolipoma from other solid

neoplasms. Angiomyolipomas can show different degrees of enhancement depending on the amount of vascularized tissue components they contain.

Oncocytoma

Oncocytomas account for 3%–7% of solid renal masses (45). They may be multicentric, bilateral, or metachronous in a minority of cases. At gross examination, the cut surface of oncocytomas is generally tan to mahogany brown or dark red, compared with the typical yellow coloration of RCC (45). A stellate central area of fibrosis or hyalinized connective tissue with compressed blood vessels, the so-called central scar, is observed in up to 54% of cases (15,46). At microscopic analysis, uniform round or polygonal eosinophilic cells (oncocytes) arranged in a variety of growth patterns predominate, but cellular atypia and pleomorphism are sometimes found. Oncocytomas are considered benign neoplasms.

The MR imaging appearance of oncocytomas is variable and nonspecific. Oncocytomas are typically spheric and well-defined masses. Relative to the renal cortex, they have lower signal intensity on T1-weighted images in approximately 70% of cases (47) and higher signal

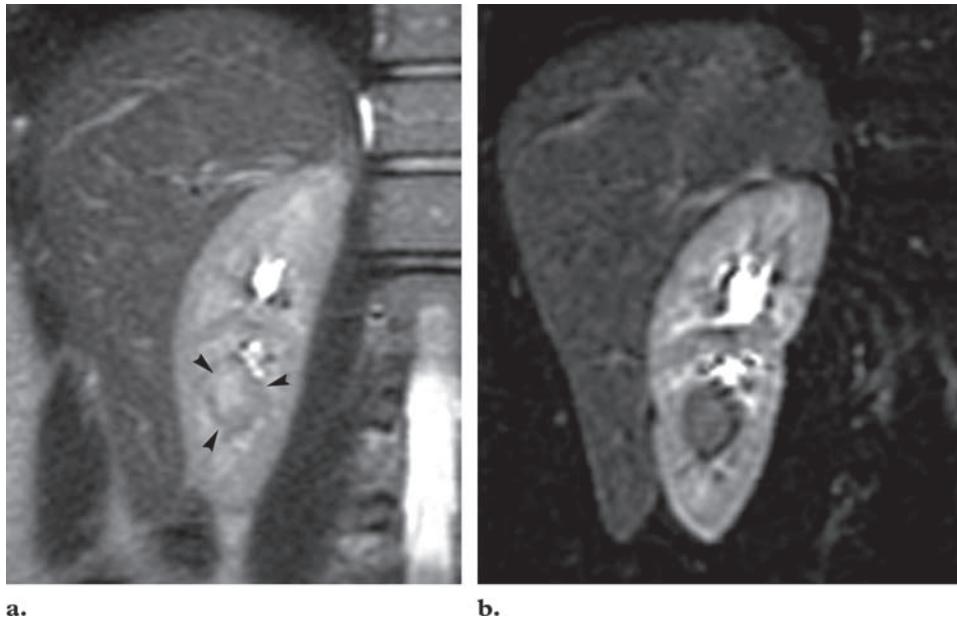


Figure 15. Juxtaglomerular cell tumor (reninoma) in a 27-year-old woman with hypertension. **(a)** Coronal steady-state fast spin-echo T2-weighted MR image shows a small mass (arrowheads) in the central portion of the right kidney. The mass was almost imperceptible during the corticomedullary and nephrographic phases, when it enhanced to the same degree as the renal medulla. **(b)** On a coronal contrast-enhanced delayed excretory phase image, the mass is homogeneous and demonstrates lower signal intensity than that of the adjacent renal parenchyma. Although the imaging findings of a hypovascular central mass are nonspecific, a clinical manifestation of hypertension is helpful, and the possibility of reninoma should be considered.

intensity on T2-weighted images in up to 67% (47). The central scar (when present) can be seen as a stellate area of low signal intensity on T1-weighted images and high signal intensity on T2-weighted images (Fig 14) (48). A well-defined hypointense capsule can be seen surrounding the tumor in almost one-half of renal oncocyomas (47). However, the presence of a pseudocapsule is nonspecific and can be seen in up to 60% of RCCs as well (49). In our experience, the central scar may show delayed enhancement after the administration of gadolinium-based contrast material.

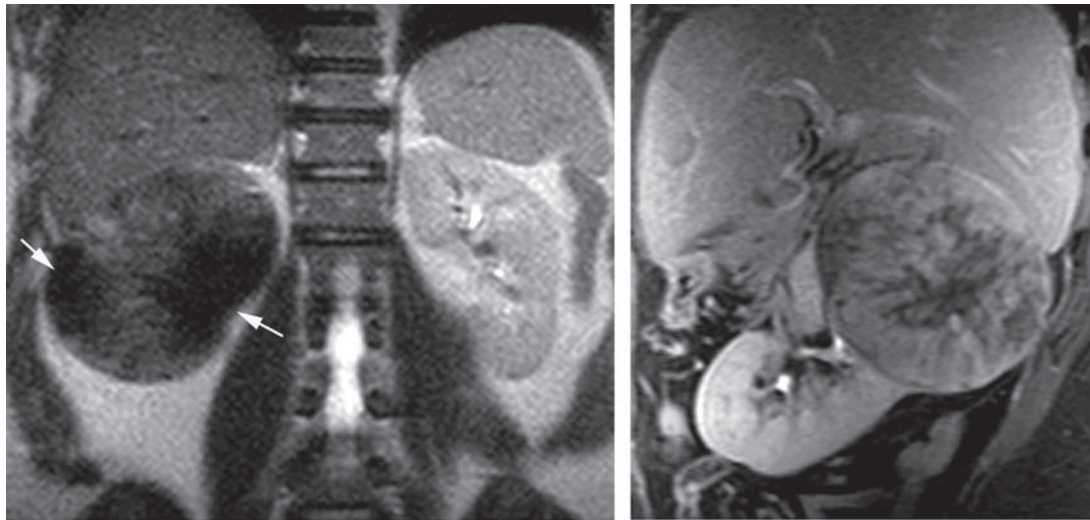
Juxtaglomerular Cell Tumor (Reninoma)

Juxtaglomerular cell tumors (reninomas) are rare benign lesions derived from the juxtaglomerular cell that occur predominantly in women in the 3rd or 4th decade of life. The clinical presentation includes hypertension with hypokalemia due

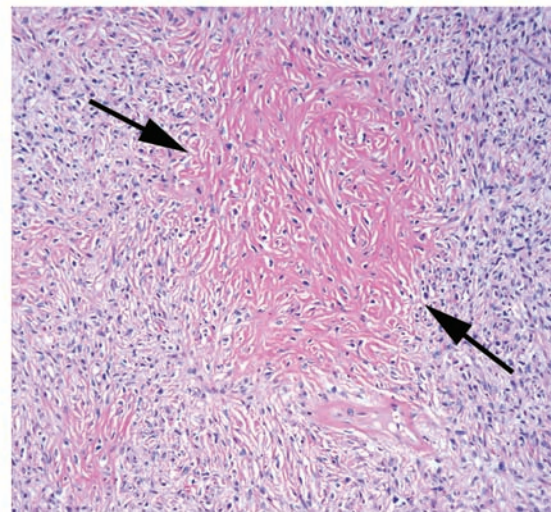
to renin hypersecretion. The diagnosis should be considered when hyperreninemia is present in the absence of renal artery stenosis.

On cut section, these masses are tan or gray and may show foci of hemorrhage. At histologic analysis, juxtaglomerular cell tumors are composed of sheets or trabeculae of round to polygonal cells. Well-developed tubules may also be present in the tumor (50). Electron microscopy can demonstrate the characteristic renin granules (51).

MR imaging typically shows a small (<3-cm) solitary mass that is hypointense on precontrast T1-weighted images. These tumors can be hypointense relative to the renal parenchyma on T2-weighted images (52). Low-level enhancement has been described after the administration of gadolinium-based contrast material (Fig 15) (53).



a.
Figure 16. Solitary fibrous tumor of the renal capsule in a 51-year-old woman. **(a)** Coronal steady-state fast spin-echo T2-weighted MR image shows a large, well-defined mass (arrows) with predominantly low signal intensity. **(b)** Oblique sagittal contrast-enhanced excretory phase fat-suppressed T1-weighted MR image shows the mass with heterogeneous enhancement, although no central necrosis is appreciated. **(c)** Photomicrograph (original magnification, $\times 10$; H-E stain) shows a neoplasm composed of a relatively monotonous proliferation of spindle cells within a collagenous, focally hyalinized stroma (arrows). “Staghorn” vessels were present elsewhere. These findings are consistent with a solitary fibrous tumor of the renal capsule.



c.

Solitary Fibrous Tumor

Solitary fibrous tumors are spindle cell neoplasms that most commonly arise in the pleura but have been described in many other locations. In the kidney, solitary fibrous tumors originate from the renal capsule. Most are benign, but malignancy is seen in 12%–23% of cases (54). These neoplasms are typically large, homogeneous, well-circumscribed firm masses. At histopathologic analysis, there is dense collagenization and fibrosis with a characteristic dispersion of the spindle cells along elongated dense collagen fibers in what has been called the “patternless” pattern (55,56). Necrosis and cystic changes are uncommon.

MR imaging shows a large, well-circumscribed mass, which is predominantly hypointense on T2-weighted images (57) and homogeneous and isointense relative to the renal capsule on T1-weighted images. Necrosis or cystic areas within

the mass, retroperitoneal collateral vessels, or enlarged lymph nodes are usually absent despite the large size of the mass (57). These tumors are relatively hypovascular; enhancement is limited during the arterial phase and tends to be heterogeneous in the delayed phase (Fig 16) (57).

Xanthogranulomatous Pyelonephritis

Xanthogranulomatous pyelonephritis is an uncommon entity that results from severe chronic infection causing diffuse renal destruction and may be misdiagnosed as a tumor. The inflammatory process extends outside the kidney to the perinephric fat and may extend further in the retroperitoneum and to the abdominal wall. *Proteus* species and *Escherichia coli* are commonly associated organisms. Risk factors include female gender and diabetes. Most patients have nephrolithiasis, and staghorn calculi are found in approximately one-half of patients.

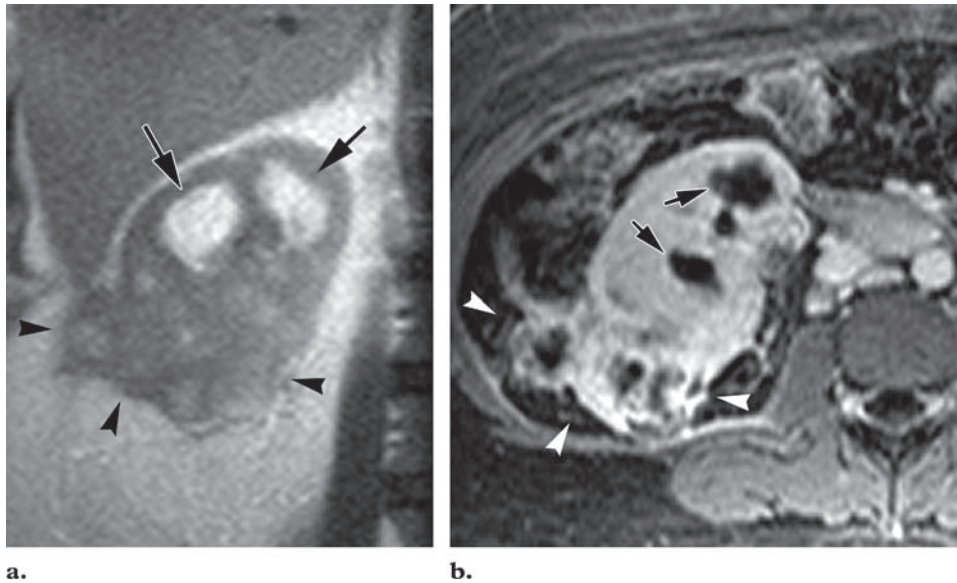


Figure 17. Xanthogranulomatous pyelonephritis in a 32-year-old woman with diabetes and *Proteus* infection of the urinary tract. **(a)** Coronal steady-state fast spin-echo T2-weighted MR image shows a poorly defined mass (arrowheads) in the lower pole of the right kidney and hydronephrosis (arrows) in the upper pole. **(b)** Axial contrast-enhanced 3D nephrographic phase fat-saturated GRE T1-weighted MR image shows irregular areas of enhancement extending into the perinephric space (arrowheads). The hypointense areas in the central region of the kidney (arrows) correspond to portions of a large staghorn calculus, which was better visualized at unenhanced CT. The appropriate clinical history and characteristic imaging findings strongly suggest the diagnosis of xanthogranulomatous pyelonephritis, which was confirmed at nephrectomy in this case.

Diffuse and focal (“tumefactive”) forms of the disease have been reported. The diffuse form is characterized by extensive involvement of the renal parenchyma and is the more common form (58). Gross examination reveals massive renal enlargement, lithiasis, peripelvic fibrosis, hydronephrosis, and lobulated yellow masses replacing renal parenchyma (59). The focal (tumefactive) form manifests as a focal renal mass of yellow tissue with regional necrosis and hemorrhage mimicking RCC (59,60).

At MR imaging, the renal parenchyma is compressed by dilated calices and replaced by abscess cavities with intermediate signal intensity on T1-weighted images and high signal intensity on T2-weighted images. Cavity walls may show marked enhancement after contrast material administration. Calculi are better depicted with CT but may be seen at MR imaging as areas of signal void within the collecting system. Although the focal form of the disease may be misinterpreted as a renal neoplasm, the presence of a staghorn calculus, appropriate clinical presentation (eg, chronic pyelonephritis in diabetic patients), and the characteristic imaging findings strongly suggest the diagnosis (Fig 17).

Conclusions

Renal masses can have distinct features at MR imaging. Recognition of some of these features may allow characterization of common and uncommon renal masses. MR imaging can be used to facilitate clinical management in patients with renal masses by depicting certain lesions that do not require treatment, providing a safe method for longitudinal follow-up, and suggesting specific surgical approaches.

References

1. Zhang J, Pedrosa I, Rofsky NM. MR techniques for renal imaging. *Radiol Clin North Am* 2003; 41:877–907.
2. Marks B, Mitchell DG, Simelaro JP. Breath-holding in healthy and pulmonary-compromised populations: effects of hyperventilation and oxygen inspiration. *J Magn Reson Imaging* 1997;7:595–597.
3. Rofsky NM, Bosniak MA. MR imaging in the evaluation of small (< or =3.0 cm) renal masses. *Magn Reson Imaging Clin N Am* 1997;5:67–81.
4. Mosetti MA, Leonardou P, Motohara T, Kanematsu M, Armao D, Semelka RC. Autosomal dominant polycystic kidney disease: MR imaging evaluation using current techniques. *J Magn Reson Imaging* 2003;18:210–215.

5. Rofsky NM, Lee VS, Laub G, et al. Abdominal MR imaging with a volumetric interpolated breath-hold examination. *Radiology* 1999;212:876–884.
6. Earls JP, Rofsky NM, DeCorato DR, Krinsky GA, Weinreb JC. Hepatic arterial-phase dynamic gadolinium-enhanced MR imaging: optimization with a test examination and a power injector. *Radiology* 1997;202:268–273.
7. Bostwick DG, Murphy GP. Diagnosis and prognosis of renal cell carcinoma: highlights from an international consensus workshop. *Semin Urol Oncol* 1998;16:46–52.
8. Chevillet JC, Lohse CM, Zincke H, Weaver AL, Blute ML. Comparisons of outcome and prognostic features among histologic subtypes of renal cell carcinoma. *Am J Surg Pathol* 2003;27:612–624.
9. Hartman DS, Davis CJ Jr, Johns T, Goldman SM. Cystic renal cell carcinoma. *Urology* 1986;28:145–153.
10. Hayakawa M, Hatano T, Tsuji A, Nakajima F, Ogawa Y. Patients with renal cysts associated with renal cell carcinoma and the clinical implications of cyst puncture: a study of 223 cases. *Urology* 1996;47:643–646.
11. Novara G, Martignoni G, Artibani W, Ficarra V. Grading systems in renal cell carcinoma. *J Urol* 2007;177:430–436.
12. Beck SD, Patel MI, Snyder ME, et al. Effect of papillary and chromophobe cell type on disease-free survival after nephrectomy for renal cell carcinoma. *Ann Surg Oncol* 2004;11:71–77.
13. Outwater EK, Bhatia M, Siegelman ES, Burke MA, Mitchell DG. Lipid in renal clear cell carcinoma: detection on opposed-phase gradient-echo MR images. *Radiology* 1997;205:103–107.
14. Eilenberg SS, Lee JK, Brown J, Mirowitz SA, Tartar VM. Renal masses: evaluation with gradient-echo Gd-DTPA-enhanced dynamic MR imaging. *Radiology* 1990;176:333–338.
15. Wagner BJ. The kidney: radiologic-pathologic correlation. *Magn Reson Imaging Clin N Am* 1997;5:13–28.
16. Yamashita Y, Watanabe O, Miyazaki T, Yamamoto H, Harada M, Takahashi M. Cystic renal cell carcinoma: imaging findings with pathologic correlation. *Acta Radiol* 1994;35:19–24.
17. Leroy X, Zini L, Leteurtre E, et al. Morphologic subtyping of papillary renal cell carcinoma: correlation with prognosis and differential expression of MUC1 between the two subtypes. *Mod Pathol* 2002;15:1126–1130.
18. Delahunt B, Eble JN. Papillary renal cell carcinoma: a clinicopathologic and immunohistochemical study of 105 tumors. *Mod Pathol* 1997;10:537–544.
19. Roy C, Sauer B, Lindner V, Lang H, Saussine C, Jacqmin D. MR Imaging of papillary renal neoplasms: potential application for characterization of small renal masses. *Eur Radiol* 2007;17:193–200.
20. Yoshimitsu K, Kakihara D, Irie H, et al. Papillary renal carcinoma: diagnostic approach by chemical shift gradient-echo and echo-planar MR imaging. *J Magn Reson Imaging* 2006;23:339–344.
21. Motzer RJ, Bander NH, Nanus DM. Renal-cell carcinoma. *N Engl J Med* 1996;335:865–875.
22. Reuter VE, Tickoo SK. Adult renal tumors. Philadelphia, Pa: Lippincott Williams & Wilkins, 2004.
23. Pickhardt PJ, Lonergan GJ, Davis CJ Jr, Kashitani N, Wagner BJ. From the archives of the AFIP: infiltrative renal lesions—radiologic-pathologic correlation. *RadioGraphics* 2000;20:215–243.
24. Holmang S, Johansson SL. Urothelial carcinoma of the upper urinary tract: comparison between the WHO/ISUP 1998 consensus classification and WHO 1999 classification system. *Urology* 2005;66:274–278.
25. Johansson S, Angervall L, Bengtsson U, Wahlqvist L. A clinicopathologic and prognostic study of epithelial tumors of the renal pelvis. *Cancer* 1976;37:1376–1383.
26. Ozsahin M, Zouhair A, Villa S, et al. Prognostic factors in urothelial renal pelvis and ureter tumours: a multicentre Rare Cancer Network study. *Eur J Cancer* 1999;35:738–743.
27. Hulnick DH, Bosniak MA. “Faceless kidney”: CT sign of renal duplicity. *J Comput Assist Tomogr* 1986;10:771–772.
28. Daniels RE 3rd. The goblet sign. *Radiology* 1999;210:737–738.
29. Hartman DS, David CJ Jr, Goldman SM, Friedman AC, Fritzsche P. Renal lymphoma: radiologic-pathologic correlation of 21 cases. *Radiology* 1982;144:759–766.
30. Urban BA, Fishman EK. Renal lymphoma: CT patterns with emphasis on helical CT. *RadioGraphics* 2000;20:197–212.
31. Heiken JP, Gold RP, Schnur MJ, King DL, Bashist B, Glazer HS. Computed tomography of renal lymphoma with ultrasound correlation. *J Comput Assist Tomogr* 1983;7:245–250.
32. Jafri SZ, Bree RL, Amendola MA, et al. CT of renal and perirenal non-Hodgkin lymphoma. *AJR Am J Roentgenol* 1982;138:1101–1105.
33. Cohan RH, Dunnick NR, Leder RA, Baker ME. Computed tomography of renal lymphoma. *J Comput Assist Tomogr* 1990;14:933–938.

34. Imai Y, Sone S, Serizawa S, et al. Magnetic resonance imaging of renal lymphoma with computed tomography correlation [in Japanese]. *Nippon Igaku Hoshasen Gakkai Zasshi* 1995;55:562-568.
35. Semelka RC, Kelekis NL, Burdeny DA, Mitchell DG, Brown JJ, Siegelman ES. Renal lymphoma: demonstration by MR imaging. *AJR Am J Roentgenol* 1996;166:823-827.
36. Dunnick N, Sandler C, Amis E, et al. *Textbook of urology*. 2nd ed. Baltimore, Md: Williams & Wilkins, 1997.
37. Clark PE, Novick AC. Exophytic noninvasive growth pattern of renal angiomyolipomas: implications for nephron sparing surgery. *J Urol* 2001;165:513-514.
38. Steiner MS, Goldman SM, Fishman EK, Marshall FF. The natural history of renal angiomyolipoma. *J Urol* 1993;150:1782-1786.
39. Oesterling JE, Fishman EK, Goldman SM, Marshall FF. The management of renal angiomyolipoma. *J Urol* 1986;135:1121-1124.
40. Bosniak MA, Megibow AJ, Hulnick DH, Horii S, Raghavendra BN. CT diagnosis of renal angiomyolipoma: the importance of detecting small amounts of fat. *AJR Am J Roentgenol* 1988;151:497-501.
41. Uhlenbrock D, Fischer C, Beyer HK. Angiomyolipoma of the kidney: comparison between magnetic resonance imaging, computed tomography, and ultrasonography for diagnosis. *Acta Radiol* 1988;29:523-526.
42. Burdeny DA, Semelka RC, Kelekis NL, Reinhold C, Ascher SM. Small (< 1.5 cm) angiomyolipomas of the kidney: characterization by the combined use of in-phase and fat-attenuated MR techniques. *Magn Reson Imaging* 1997;15:141-145.
43. Israel GM, Hindman N, Hecht E, Krinsky G. The use of opposed-phase chemical shift MRI in the diagnosis of renal angiomyolipomas. *AJR Am J Roentgenol* 2005;184:1868-1872.
44. Kim JK, Kim SH, Jang YJ, et al. Renal angiomyolipoma with minimal fat: differentiation from other neoplasms at double-echo chemical shift FLASH MR imaging. *Radiology* 2006;239:174-180.
45. Kuroda N, Toi M, Hiroi M, Shuin T, Enzan H. Review of renal oncocytoma with focus on clinical and pathobiological aspects. *Histol Histopathol* 2003;18:935-942.
46. Amin MB, Crotty TB, Tickoo SK, Farrow GM. Renal oncocytoma: a reappraisal of morphologic features with clinicopathologic findings in 80 cases. *Am J Surg Pathol* 1997;21:1-12.
47. Harmon WJ, King BF, Lieber MM. Renal oncocytoma: magnetic resonance imaging characteristics. *J Urol* 1996;155:863-867.
48. Ball DS, Friedman AC, Hartman DS, Radecki PD, Caroline DF. Scar sign of renal oncocytoma: magnetic resonance imaging appearance and lack of specificity. *Urol Radiol* 1986;8:46-48.
49. Pretorius ES, Siegelman ES, Ramchandani P, Cangiano T, Banner MP. Renal neoplasms amenable to partial nephrectomy: MR imaging. *Radiology* 1999;212:28-34.
50. Kuroda N, Moriki T, Komatsu F, et al. Adult-onset giant juxtaglomerular cell tumor of the kidney. *Pathol Int* 2000;50:249-254.
51. Abbi RK, McVicar M, Teichberg S, Fish L, Kahn E. Pathologic characterization of a renin-secreting juxtaglomerular cell tumor in a child and review of the pediatric literature. *Pediatr Pathol* 1993;13:443-451.
52. Kashiwabara H, Inaba M, Itabashi A, Ishii J, Katayama S. A case of renin-producing juxtaglomerular tumor: effect of ACE inhibitor or angiotensin II receptor antagonist. *Blood Press* 1997;6:147-153.
53. Agrawal R, Jafri SZ, Gibson DP, Bis KG, Ali R. Juxtaglomerular cell tumor: MR findings. *J Comput Assist Tomogr* 1995;19:140-142.
54. Gelb AB, Simmons ML, Weidner N. Solitary fibrous tumor involving the renal capsule. *Am J Surg Pathol* 1996;20:1288-1295.
55. Wang J, Arber DA, Frankel K, Weiss LM. Large solitary fibrous tumor of the kidney: report of two cases and review of the literature. *Am J Surg Pathol* 2001;25:1194-1199.
56. England DM, Hochholzer L, McCarthy MJ. Localized benign and malignant fibrous tumors of the pleura: a clinicopathologic review of 223 cases. *Am J Surg Pathol* 1989;13:640-658.
57. Johnson TR, Pedrosa I, Goldsmith J, Dewolf WC, Rofsky NM. Magnetic resonance imaging findings in solitary fibrous tumor of the kidney. *J Comput Assist Tomogr* 2005;29:481-483.
58. Ramboer K, Oyen R, Verellen S, Vermeersch S, Baert AL, Verberckmoes R. Focal xanthogranulomatous pyelonephritis mimicking a renal tumor: CT- and MR-findings and evolution under therapy. *Nephrol Dial Transplant* 1997;12:1028-1030.
59. Hayes WS, Hartman DS, Sesterbenn IA. From the archives of the AFIP: xanthogranulomatous pyelonephritis. *RadioGraphics* 1991;11:485-498.
60. Verswijvel G, Oyen R, Van Poppel H, Roskams T. Xanthogranulomatous pyelonephritis: MRI findings in the diffuse and the focal type. *Eur Radiol* 2000;10:586-589.

MR Imaging of Renal Masses: Correlation with Findings at Surgery and Pathologic Analysis

Ivan Pedrosa, MD, et al

RadioGraphics 2008; 28:985–1003 • Published online 10.1148/rg.284065018 • Content Codes: GU MR OI

Page 986

The presence of enhancement within a renal lesion after the administration of gadolinium-based contrast material is the most reliable criterion for distinguishing solid masses from cysts at MR imaging.

Page 988

Coronal delayed 3D fat-saturated GRE T1-weighted images acquired after contrast material administration provide excellent MR urographic information for the assessment of urothelial disease.

Page 989

Loss of signal intensity within the solid portions of clear cell RCCs on opposed-phase images compared with in-phase images is due to cytoplasmic fat and has been observed in up to 60% of these tumors.

Page 993

Enhancement of a focal filling defect in the collecting system is strongly suggestive of a TCC.

Page 996

the most reliable demonstration of bulk fat within an angiomyolipoma can be achieved by comparing images obtained with the same imaging parameters before and after applying a selective fat-suppression pulse.